GSA Data Repository Item: 2007183

Data Repository Item For: Kinematics and geometry of active detachment faulting beneath the TAG hydrothermal field on the Mid-Atlantic Ridge

Brian J. deMartin[1*], Robert A. Reves-Sohn[2], Juan Pablo Canales[2], Susan E. Humphris[2]

[1]MIT/WHOI Joint Program in Oceanography, Cambridge, MA 02139, USA
[2]Woods Hole Oceanographic Institution, Woods Hole, MA 02543, USA

[*]Now at Brown University, Providence, RI 02912, USA

This file contains:

I. Sample seismograms and phase picks

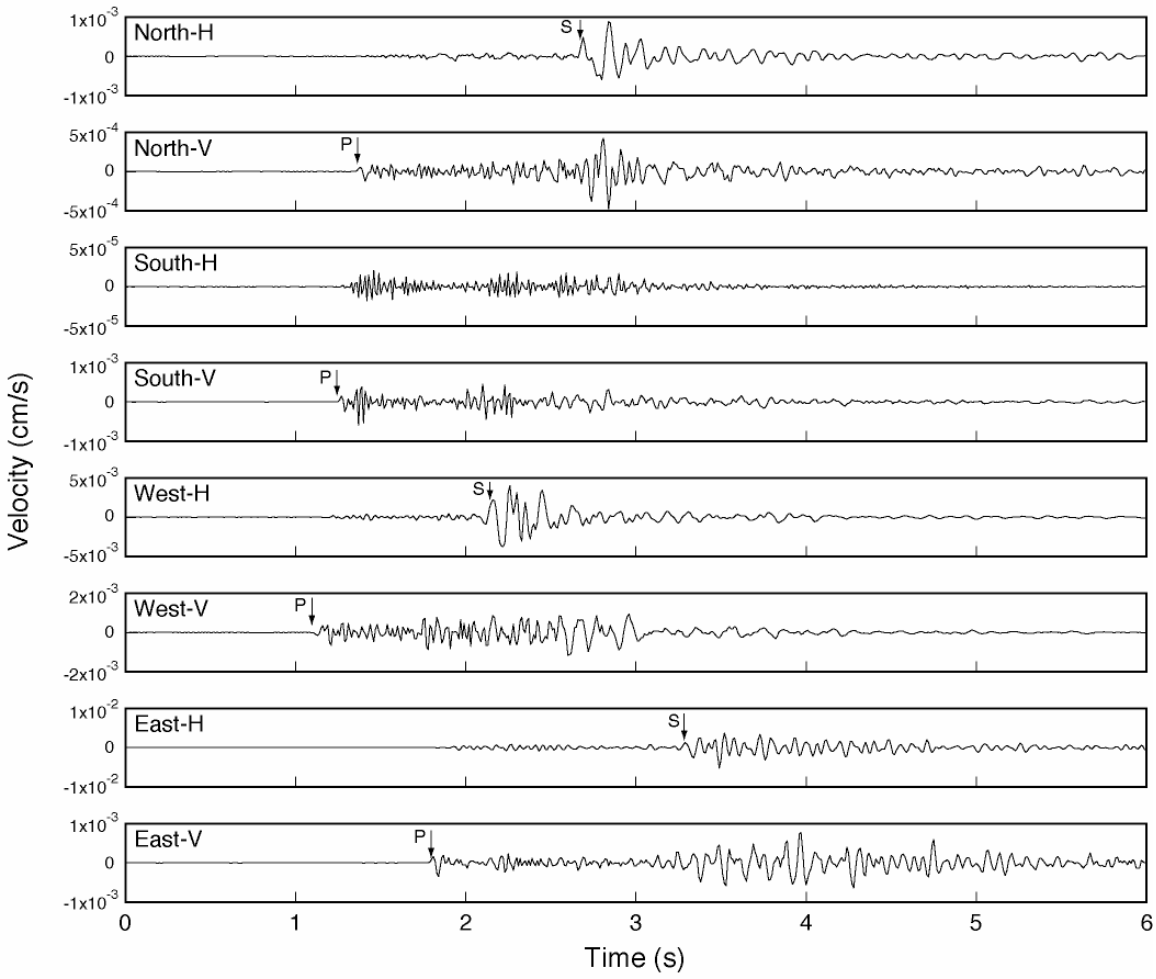

Figure DR1: Seismograms and compressional (*P*) and shear (*S*) phase picks from an event (M_L = 2.57) located on the detachment fault (at 26º 8.5'N, -44º 51.34'W, 6.5 km depth). Vertical (V) and horizontal (H) components of velocity are shown for the outermost ring of instruments in the network (i.e., North, South, East, and West instruments). Nominal arrival time uncertainties are 75 ms for *P*-waves and 150 ms for *S*-waves (note that no *S*-pick was made for the South instrument in this case). Data are band-pass filtered from 5-40 Hz.

II. Hypocenter catalog

P- and *S*- phase picks were made for 51,667 events detected by all 13 OBSs. Hypocenters were estimated via stochastic descent on a grid of rms residuals generated based on the difference between the phase picks and travel times predicted using William Menke's Raytrace3d program (Menke, 2005). Satisfactory hypocentral estimates (defined by rms residual < 0.12 s) were obtained for 19,232 events, with the rest being too far removed from the seismic network for accurate analysis. Hypocenter uncertainties were estimated at the 95% confidence interval using the method of Wilcock and Toomey (1991) as modified by Sohn et al. (1998). A hypocenter catalog in the format described in Table DR1 is available at the Marine Geoscience Data System (https://www.marine-geo.org/tools/search/Files.php?data_set_uid=6798#datasets).

Table DR1. Sample entry from hypocenter catalog.

EQ Identification Number	Time*	Hypocenter rms residual (s)	Longitude (º)	± X (km)	Latitude (º)	± Y (km)	Depth Below Sea Level (km)	± Z (km)	Moment (N m)
124210310	01/24/2004 21:03:10.11	0.0827	-44.84634	0.50	26.14168	0.75	7.250	0.75	1.899E+18

*Time string is in month/day/year hour:minute:second format.

References:

Menke, W., 2005, Case studies of seismic tomography and earthquake location in a regional context.

Sohn, R.A., Hildebrand, J.A., and Webb, S.C., 1998, Postrifting seismicity and a model for the 1993 diking event on the CoAxial segment, Juan de Fuca Ridge: J. Geophys. Res., v. 103, p. 9867-9877.

Wilcock, W.S.D., and Toomey, D.R., 1991, Estimating hypocentral uncertainties for marine microearthquake surveys: A comparison of the generalized inverse and grid search methods: Marine Geophysical Researches, v. 13, p. 161-171.

III. Composite focal plane solutions

Composite focal plane solutions provide a means to incorporate focal mechanism constraints from multiple events within a small area into a single focal plane estimate. The polarity (i.e., up or down) of the observed *P*- arrivals from a group of events is plotted on a single focal sphere, which reduces focal plane uncertainties provided the events share a common source mechanism. The composite mechanisms shown in Figure 1a were generated using *P*-wave polarity estimates from 3 sets of events; (1) 304 events on the arc of the detachment (depth interval of 4.4 to 9.0 km below sea level), (2) 543 events on the inboard (i.e., westernmost) linear trend of seismicity (depth interval of from 3.5 to 5.9 km below sea level), (3) 365 events on the outboard (i.e., easternmost) linear trend of seismicity (depth interval from 3 to 5.8 km below sea level).

IV. Active-source seismic data

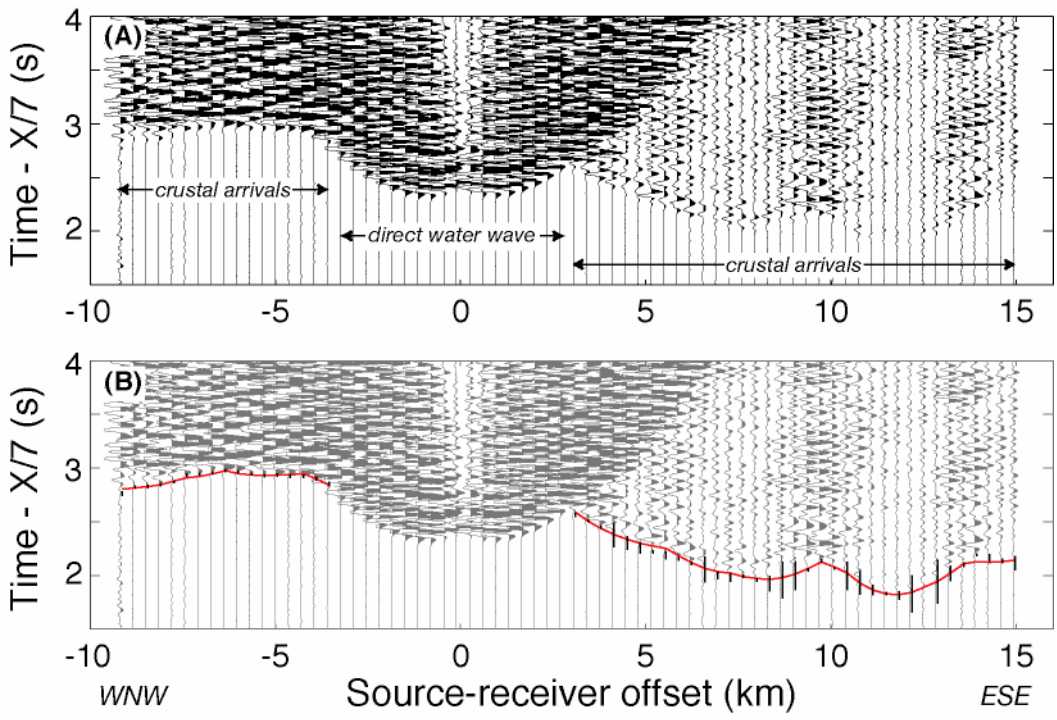

Figure DR2: (A) Example of active-source seismic record section for the OBS located 1 km to the west of the TAG mound. Vertical axis is travel time reduced to 7 km/s. Data have been band-pass filtered between 5 and 20 Hz, and amplitudes scaled according to range for display purposes. Labels indicate the nature of first arrivals at different offsets. Travel times were hand-picked, and uncertainty estimates included dependency on the signal-to-noise ratio, uncertainty in both source and receiver locations, and uncertainty in seafloor ray entry points due to out-of-plane topography. (B) Same as (A), with observed travel time picks (vertical bars with length equal to twice the assigned uncertainty) and predicted travel times (red line) by the preferred 2-D model shown in Figure 2a.

V. Tomographic resolution

We performed synthetic tests to determine the accuracy of inferring fault dip angles in the upper 3 km of the crust from the tomography model shown in Figure 2. We inverted synthetic travel times predicted by several models in which we imposed velocity anomalies resulting from extension and uplift along a fault, varying the fault dip, and then estimated the fault dip from the resulting tomography models. We found that our experiment can measure fault dips with an accuracy of ±5° if the fault dip is less than 35°. Faults dipping at steeper angles would be imaged in our tomography models with an apparent dip of 35°.

Additional tomography models along the axial valley of the TAG segment presented by Canales et al. (2005) show no evidence of low velocity zones beneath the TAG active mound. Resolution tests indicate that those tomographic inversions are capable of resolving low velocity anomalies beneath the TAG active mound with lateral dimensions ≥3 km if they are shallower than 4 km.